Characterizing Offshore Freshened Groundwater Salinity Patterns using Trans-dimensional Bayesian Inversion of Controlled Source Electromagnetic Data: A Case Study from the Canterbury Bight, New Zealand

Zahra Faghih[1], Amir Haroon[1], Marion Jegen[1], Romina Gehrmann[2], Katrin Schwalenberg[3], Aaron Micallef[4], Jan Dettmer[5], Christian Berndt[1], Joshu Mountjoy[6], Bradley A. Weymer[7]

[1] GEOMAR Helmholtz Centre for Ocean Research, Kiel, Germany.

[2] Dalhousie University, Halifax, Canada.

[3] Federal Institute for Geosciences and Natural Resources (BGR), Hanover, Germany.

[4] University of Malta, Msida, Malta.

[5] University of Calgary, Calgary, Canada.

[6] National Institute for Water and Atmospheric Research (NIWA), Wellington, New Zealand.

[7] Shanghai Jiao Tong University, Shanghai, China.

Corresponding author: Zahra Faghih (zfaghih@geomar.de)

Key Points:

- A Bayesian workflow is employed to evaluate uncertainty in pore-water salinity estimates.
- Offshore groundwater in Canterbury Bight stores freshened pore-water in fine-grained sediments, likely extending from the onshore aquifer.
- Correlation between pore-water salinities and seismic-derived stratigraphy provides boundary conditions for hydrogeological modeling.

Abstract

Although marine controlled source electromagnetic (CSEM) methods are effective for investigating offshore freshened groundwater (OFG) systems, interpreting the spatial extent and salinity of OFG remains challenging. Integrating CSEM resistivity models with information on sub-surface properties, such as host-rock porosity, allows for estimates of pore-water salinity. However, deterministic inversion approaches pose challenges in quantitatively analyzing these estimates as they provide only one best-fit model with no associated estimate of model parameter uncertainty. To address this limitation, we employ a trans-dimensional Markov-Chain Monte-Carlo inversion on marine CSEM data, under the assumption of horizontal stratification, collected from the Canterbury Bight, New Zealand. We integrate the resulting posterior distributions of electrical resistivity with borehole and seismic reflection data to quantify pore-water salinity with uncertainty estimates. The results reveal a low-salinity groundwater body in the center of the survey area at varying depths, hosted by consecutive silty- and fine-sand layers approximately 20 to 60 km from the coast. These observations support the previous study's results obtained through deterministic 2-D inversion and suggest freshening of the OFG body closer to the shore within a permeable, coarse-sand layer 40 to 150 m beneath the seafloor. This implies a potential active connection between the OFG body and the terrestrial groundwater system. We demonstrate how the Bayesian approach constrains the uncertainties in resistivity models and subsequently in pore-water salinity estimates. Our findings highlight the potential of Bayesian inversions in enhancing our understanding of OFG systems, providing crucial boundary conditions for hydrogeological modeling and sustainable water resource development.

Plain Language Summary

Geophysical methods that measure the electromagnetic properties of the Earth are effective in investigating freshwater sources beneath the seafloor. By Combing the geophysical and geological information, we can better assess the quality of this groundwater. In this study, we develop a workflow that uses statistical methods to integrate electromagnetic observations with borehole and acoustic measurements along the eastern coast of the South Island of New Zealand. We aim to improve our understanding of the groundwater quality beneath the seafloor. Our research shows the presence of freshened groundwater within the sandy seafloor. Importantly, our observations indicate that the freshwater extends closer to the coast. These findings are

54 significant as they enhance the hydrogeological modeling of the groundwater system and suggest
55 its potential as a source of freshwater.

56 ## 1 Introduction

57 The rising demand for potable water in coastal regions has recently promoted growing
58 research interest in detecting offshore freshened groundwater (OFG) worldwide (Post et al.,
59 2013). OFG emplacement is commonly explained through either meteoric recharge during sea-
60 level low-stands (e.g., Cohen et al., 2010; Meisler, Leahy, & Knobel, 1984; Person et al., 2003)
61 and/or through active meteoric recharge via permeable connections between onshore and
62 offshore aquifers (e.g., Hong et al., 2019; Johnston, 1983; Weymer et al., 2022), allowing
63 freshened pore-fluid to reside within presently submerged seafloor. Due to the ongoing pressure
64 on terrestrial aquifers caused by environmental and anthropogenic stressors, offshore
65 groundwater investigation has gained new urgency. One proposition is that near-coastal OFG
66 reservoirs can serve as unconventional sources of drinking water, especially along densely
67 populated coastal regions and on islands, where terrestrial aquifers cannot maintain a sufficient
68 supply for inhabitants, agriculture, and industry (Bakkenet al., 2012; Micallef et al., 2021;
69 Zamrsky, Essink et al., 2022).

70 Evidence of OFG has been documented in coastal embayments and continental shelves
71 worldwide (e.g., Attias et al., 2020; Cambareri & Eichner, 1998; Gustafson et al., 2019; Haroon,
72 Lippert et al., 2018; Haroon et al., 2021; Hathaway et al., 1979; King et al, 2022; Martin et al.,
73 2007; Micallef et al., 2020), demonstrating that low-salinity groundwater within the seafloor
74 (water depths <1000 m) occurs on a global scale (Post et al., 2013). Global OFG volume has
75 been estimated at 106 km3 (Micallef et al., 2021), yet these estimates are poorly constrained
76 since they are based on first-order assumptions derived from point-source borehole
77 measurements and hydrogeological modeling. A general lack of integrated geophysical data and
78 hydrogeological investigations along continental shelves precludes a seamless accounting for
79 more precise volume and salinity estimates on both global and regional scales (Weymer et al.,
80 2022). In order to argue for the sustainable use of OFG as an unconventional resource, volumes,
81 geometries, salinities, as well as environmental impacts need to be precisely quantified before
82 exploitation.

Several applications of marine controlled source electromagnetic (CSEM) methods have proven effective in identifying OFG residing in various offshore geological settings (e.g., Attias et al., 2020; Blatter et al., 2019; Evans, 2007; Gustafson et al., 2019; Haroon, Lippert et al., 2018; Haroon et al., 2021; King et al., 2022; Levi et al., 2018; Lippert & Tezkan, 2020; Micallef et al., 2020). The electrical resistivity distribution of the seafloor, which can be obtained from CSEM data, is controlled by the salinity of the pore-fluid, the porosity of the host rock, and the degree of its cementation (Archie, 1942; Hoefel & Evans, 2001). Thereby, resistivity models are utilized as a proxy to delineate the spatial extent of OFG systems along continental shelves by applying the empirical Archie's relationship (Archie, 1942) which relates the resistivity of the seafloor to the resistivity of the pore-fluid (e.g., Gustafson et al., 2019; King et al., 2022; Micallef et al., 2020), but only one study assesses the uncertainty of the derived resistivity models and its impact on the uncertainty of OFG reservoir characterization (Blatter et al., 2019). This is particularly important when aiming to validate hydrogeological models with geophysical data, an approach that has been identified as instrumental in the future assessment of OFG resource potential, evolution, and response functions to external drivers (Arévalo-Martínez et al., 2023; Weymer et al., 2022).

From a geophysical perspective, one of the main challenges in the assessment of OFG bodies is to reliably predict the pore-fluid salinity distribution based on electrical resistivity models. Two primary factors contribute to uncertainty in the OFG salinity estimation: a) the uncertainty of the best-fit resistivity model, and b) unknown variations in lithology-dependent parameters in Archie's relationship. The majority of CSEM studies apply a smoothness constraint in a deterministic inversion approach and subsequently estimate pore-fluid salinities by assuming representative values for the cementation factor and host-rock porosity in Archie's relationship (Archie, 1942). In most cases, the comparison between predicted salinity distributions derived from geophysical models and hydrogeological modeling or ground-truth measurements at boreholes achieves only a qualitative match (e.g., Gustafson et al., 2019; Micallef et al., 2020), possibly because model parameter ambiguities do not flow into the analysis. A more quantitative assessment of OFG salinity distributions can be achieved if uncertainties are addressed within the entire evaluation chain of deriving pore-water salinity models from integrated CSEM analysis.

An uncertainty evaluation of pore-water salinity predictions derived from CSEM measurements will allow inference about the genesis of OFG and its potential connection to their terrestrial counterparts, as well as provide a cornerstone for future monitoring of freshwater/saltwater interfaces with electromagnetic methods. These uncertainty estimates ideally require a statistical analysis of all parameters in Archie's empirical relationship (Archie, 1942), i.e., bulk resistivity, porosity, and cementation factor. Deterministic CSEM inversion approaches use an objective function that is constrained by additional regularization terms such as a roughness constraint (e.g., Constable et al., 1987) to iteratively optimize the data misfit between measured and synthetic data and ensure numerical stability. These deterministic inversion approaches are computationally efficient in terms of searching for one best-fit model (e.g., Abubakar et al., 2008; Constable et al., 1987) and therefore required for a 2-D and 3-D inversion of CSEM data. Yet, they cannot quantify the inherent uncertainty in model parameters. Moreover, smoothed resistivity models pose additional challenges when integrated with other geophysical data, such as multi-channel seismic (MCS) reflection or borehole data, due to disparate spatial resolution. However, integrating electrical resistivity models with lithological information derived from seismic/acoustic methods is essential for the regional mapping of OFG (e.g., Weymer et al., 2022), as lithological sequences and geological heterogeneities govern the distribution of OFG (Zamrsky, Karssenberg, et al., 2020). In contrast to deterministic inversion approaches, Bayesian inversion algorithms treat parameters as random variables that are probabilistically sampled, resulting in an ensemble of best-fit resistivity models instead of a single best-fit model. Therefore, they can be used to provide rigorous estimates of model parameter uncertainties (Malinverno, 2002); however, the large computation time associated with them limits their application to 1-D modeling. Trans-dimensional Bayesian inversion has been applied to various geophysical data (e.g., Bodin & Sambridge, 2009; Dettmer, Dosso, & Holland, 2011; Gallagher, 2012; Ray, Alumbaugh, et al., 2013).

The goal of this study is to introduce a workflow using a 1-D Bayesian inversion to evaluate uncertainty in pore-water salinity predictions derived from integrated analysis based on CSEM, MCS, and borehole data. We base our analysis on a data set acquired in the Canterbury Bight, NZ (cf. Figure 1), where all required data are available and an OFG body is known to exist within the shallow seafloor (Micallef et al., 2020). Firstly, we validate the developed workflow at the site of borehole U1353 drilled during IODP Expedition 317 (Fulthorpe et al.,

144 2011) for ground-truthing and subsequently apply it at locations further away from the borehole,
145 where the aquifer response detected by CSEM is greatest. Lastly, we discuss insights gained
146 from this analysis regarding the evolution of Canterbury Bight's OFG system.

147 **2 Regional Setting and Available Data**

148 Canterbury Bight is located along the eastern coast of the South Island of New Zealand.
149 The continental shelf, spanning an approximate area of 13000 km2, includes about 1 km-thick
150 progradational successions of shelf-slope deposits (e.g., Browne & Naish, 2003; Lu & Fulthorpe,
151 2003). To determine the relative contributions of global sea level fluctuations (eustasy) and local
152 tectonic, sedimentary, and oceanographic processes in controlling continental margin
153 depositional cyclicity, three International Ocean Discovery Program (IODP) sites were drilled
154 along a coast perpendicular transect during IODP Expedition 317 (Fulthorpe et al., 2011; Figure
155 1a). A subtle decrease in pore-water salinity was observed at Site U1353, which is located
156 closest to the shoreline at a water depth of 85 m and a distance of about 45 km from the coast.
157 This salinity anomaly was identified at a depth between 20 m and 60 m below the seafloor (bsf)
158 and contains brackish pore-water with a salinity of approximately 24 practical salinity units
159 (psu), in contrast to the background seawater salinity of 34 psu in the survey area (Micallef et al.,
160 2020).

161 In 2018, a joint marine CSEM and seismic survey was conducted within the framework
162 of the MARCAN project. The survey covered four profiles spanning a total length of 175 km
163 across the Canterbury Bight and utilized a seafloor-towed CSEM system. This system employed
164 a 100 m long transmitter dipole with a 20 A bipolar current signal and four inline electric field
165 receiver dipoles (Gehrmann, Dettmer, et al., 2015) with offsets of 150 m, 250 m, 400 m, and 650
166 m. The CSEM measurements were obtained at 267 stationary waypoints spaced every 500 m
167 along lines 2, 4, and 5, and every 1 km along line 7, at a sampling rate of 10 kHz. Collected MCS
168 data was acquired using a GeoEel Digital seismic streamer (Geometrics). The streamer consisted
169 of 24 channels with a group interval of 12.5 m and offsets between 22 m and 308 m. The seismic
170 source was a single mini GI-gun (13/35 cubic inch) towed at 1.5 m below the sea-surface.

171 Resistivity models derived from a 2-D deterministic inversion of the acquired CSEM data
172 are presented by Micallef et al. (2020) using a time-domain extension of MARE2DEM (Haroon,
173 Hölz, et al., 2018; Key, 2016). Moreover, Micallef et al. (2020) interpreted the MCS reflection

profiles in terms of geological facies clay, silt, fine sand, coarse sand, and gravel, respectively. For conducting hydrogeological modeling, they assigned porosities of 45 percent to clay and silty material, 40 percent to fine sands, 35 percent to coarse sands, and 20 percent to gravel. However, it is important to note that these values represent mean first-order estimates, and their uncertainty is likely to increase at greater distances from the borehole U1353. This is due to limitations in the interpretation bias in seismic facies classification, inadequate information on sediment sorting and compaction, and local heterogeneities.

According to Micallef et al. (2020), the most prominent resistivity anomaly (> 25 Ωm) is identified north of the borehole on the coast perpendicular line 4 and along the coast parallel line 7 (cf., Figure 4 in Micallef et al., 2020) This anomaly is significant as marine sediments in the region typically exhibit resistivity values ranging from 0.3 Ωm to 3 Ωm when fully saturated with seawater (Fulthorpe et al., 2011). Therefore, the identified resistivity anomalies suggest the presence of a large OFG body to the north of the borehole. The results of Micallef et al. (2020) also indicate that site U1353 serves as the southern boundary of a substantial OFG system that extends northwards up to line 5. Micallef et al. (2020) estimated pore-water salinities from the 2-D resistivity models by applying Archie's relationship assuming constant porosities of 20, 30, and 40 percent to define plausible upper and lower limits of the potential OFG volumes. Their results suggest that the volume of OFG may increase by a factor of four as porosity increases from 20 to 40 percent.

To enhance the accuracy of the salinity estimates and address associated uncertainties, we selected waypoints on line 2, intersecting with the borehole, and on line 4, which features the identified resistivity anomaly, for a Bayesian analysis. The workflow of this analysis is explained in the following section.

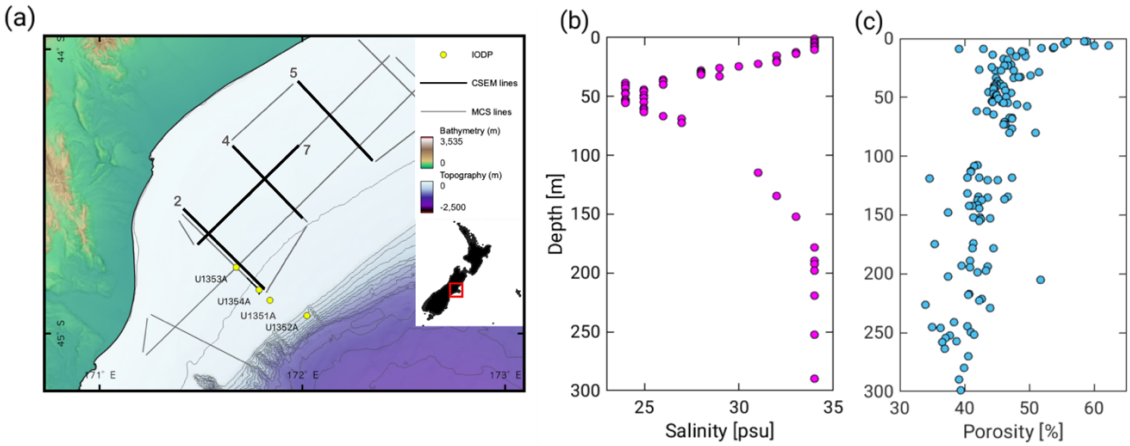

Figure 1. (a) Map of the Canterbury Basin displaying the locations of acquired CSEM and seismic profiles. The yellow circles illustrate the locations of the IODP boreholes. CSEM line 2 intersects with the location of IODP site U1353, for which (b) salinity and (c) porosity measurements up to a depth of 300 mbsf are available (Fulthorpe et al., 2011)

3 Methods

To quantify pore-water salinity with corresponding uncertainty estimates using CSEM data, we employ a 1-D trans-dimensional Markov Chain Monte Carlo (MCMC) modeling approach (e.g., Mosegaard & Tarantola, 1995; Sambridge & Mosegaard, 2002) based on a Metropolis-Hastings algorithm (Green, 1995; Hastings, 1970; Metropolis et al., 1953). Following the concepts of previous publications (Blatter et al., 2019; Gehrmann, Dettmer, et al., 2015; Gehrmann, Schwalenberg, et al., 2015; Ray & Key, 2012), we compute the posterior probability density (PPD) of resistivity models that are constrained by measured CSEM data and independent prior information about the site. These probabilities are then converted to probabilities of pore-water salinity by applying Archie's relationship (Archie, 1942).

3.1 Bayesian formulation

Here, Bayesian inversion employs MCMC sampling to estimate the PPD. The computational cost for Bayesian inversion can be large and therefore limits its applications mainly to 1-D layered resistivity models that are computationally less expensive compared to 2-D/3-D modeling. However, the predominantly horizontal stratigraphy observed in the CSEM experiment's scale enables a 1-D inversion.

The PPD combines prior knowledge about the model parameters and data information (e.g., Gelman et al., 2014), as expressed by Bayes' theorem.

$$p(\mathbf{m}|\mathbf{d}) = \frac{p(\mathbf{d}|\mathbf{m})p(\mathbf{m})}{p(\mathbf{d})}, \quad (1)$$

where **d** and **m** are the vectors of data and model parameters, respectively, and p represents the probability density functions (PDF). The PPD is the conditional probability of model parameters given the observed data, $p(\mathbf{m}|\mathbf{d})$. The term $p(\mathbf{d}|\mathbf{m})$ is the conditional probability of the data given the model, which is interpreted as the likelihood of the model, $L(\mathbf{m})$, for observed data. The prior $p(\mathbf{m})$ is a probability density function of model parameters and is independent of the data. In this study, uniform distributions with parameter bounds are chosen as priors so that the solution is primarily constrained by the data. The probability $p(\mathbf{d})$ is the Bayesian evidence and normalizes the probability to unity. It can be ignored in this work (e.g., Sambridge et al., 2006).

For the likelihood function $L(\mathbf{m})$, we assume that data errors are zero-mean and Gaussian distributed with covariance matrix $\mathbf{C}_d$, see equation. (2), where χ^2 is the data misfit, equation (3),

$$p(\mathbf{d}|\mathbf{m}) \propto \exp\left(-\frac{\chi^2}{2}\right), \quad (2)$$

where χ^2quantifies the fit of predicted data $f(\mathbf{m})$ and observed data **d**.

$$\chi^2 = \big(\mathbf{d} - f(\mathbf{m})\big)^T \mathbf{C}_d^{-1} \big(\mathbf{d} - f(\mathbf{m})\big). \quad (3)$$

In this study, we use 1-D trans-dimensional MCMC algorithm with parallel tempering (Dettmer & Dosso, 2012), which efficiently samples the parameter space by incorporating a variable number of sub-seafloor resistivity layers. The algorithm adds and deletes layers depending on the data required using the Metropolis-Hastings-Green acceptance criterion (Metropolis et al., 1953). To improve the starting model for MCMC sampling, we use a non-linear hybrid optimization technique (Dosso et al., 2001)

The PPD relies on the selection of appropriate data errors and minimum errors. If the data errors are large, the model resolution will decline, leading to large uncertainties. Conversely, small data errors can cause overfitting, resulting in unrealistically low uncertainty. Here, we assign a minimum relative error of one percent to account for systematic errors such as

inaccurate array geometry or timing errors between transmitter and receiver signals. The one percent value is close to the data error derived during the CSEM data processing step, stacking. It is important to note that the applied minimum errors are smaller than the minimum allowed relative errors of four percent that were assumed for the deterministic 2-D inversion in Micallef et al. (2020; Figure 2a). This larger error was employed in the 2-D inversion as it searches for a vertically and laterally smoothed model over all data collected along the profile, whereas a 1-D layered model uses only data measured at one predefined waypoint. To better understand the impact of the applied error model on the PPDs and allow for a more coherent comparison with the 2-D inversion, we also provide PPDs for an assumed minimum error of four percent in the appendix (cf., Figure A 1).

3.2 Probability density of resistivity models

Inherent to CSEM data inversion is that the product between resistivity and layer thickness is often better resolved than the parameters themselves (Edwards, 1997). One major advantage of implementing a trans-dimensional inversion is therefore the assessment of the uncertainty of the resistivity and the layer thickness. We present these in terms of interface probabilities as a function of depth (Figure 2b, left) and PPD profiles for a layered sub-seafloor resistivity (Figure 2b, right). To illustrate the PPDs, we create depth grids and generate normalized histograms for resistivity values at predefined depth intervals (Figure 2b). The histogram values within each depth bin represent the corresponding probability density with higher values indicating a higher probability, represented by warmer colors. Cooler and grey colors represent low probability density while white indicates no models within the grid cell. The posterior median model is presented by a dashed black line, and the uncertainties in the model parameters are quantified with 95 percent credibility intervals (CI). To show the Bayesian results as interface-depth probabilities, we create a depth grid and calculate normalized histograms for the number of interfaces estimated at each depth interval. Additionally, to facilitate comparison we extract resistivity-depth profiles from the 2-D inversion of Micallef et al. (2020) at the collected locations (represented by black circular markers).

3.3 Conversion of resistivity to pore-water salinity probability distribution

After obtaining the ensemble of seafloor resistivity models through Bayesian inversion, we convert them into pore-fluid salinity values using the Fofonoff & Millard (1983) algorithm. We then apply Archie's relationship (Archie, 1942) to link the bulk resistivity (ρ_b) to the pore-fluid resistivity (ρ_f) using the following equation.

$$\rho_b = a\phi^{-m}\rho_f. \quad (4)$$

Here, ϕ is the porosity of sediments, a is the tortuosity factor and m is the formation cementation factor, indicating the degree of interconnection of the pore spaces and generally assumed to be constant for a given geological structure. Pore-water salinity can be derived from pore-water resistivity, temperature, and pressure based on the Practical Salinity Scale (PSS –78) conversion (Fofonoff & Millard, 1983). We assume that porosity values at each depth are normally distributed, with a standard deviation of 0.05. Our incomplete knowledge of Archie's parameter coefficients a and m is encapsulated in the workflow by assuming a uniform distribution in the range of 0.8 to 1.2 and 1.9 to 2.3, respectively. This uniform distribution best captures the variation in Archie's parameters due to interbedding of silty and sandy material, which has been observed in the borehole core and seismic data (cf., Figure 3).

At the borehole U1353 location, porosity values obtained from in-situ measurements are available (Fulthorpe et al., 2011). For locations away from the borehole, we extract the porosity-depth profile at any desired waypoint from the seismically interpreted facies presented by Micallef et al. (2020; Figure 3) along the survey lines. To compute pore-water salinity distributions as a function of depth, we generate a salinity-depth grid with a vertical resolution of 5 m and translate the ensemble of resistivity models onto the grids. At each depth interval, a random generator selects corresponding ρ_b, ϕ, m, and *2* values from the individual distributions to obtain ρ_f, which is subsequently converted into a pore-water salinity profile. Normalized histograms of the salinity distributions at each depth interval are computed and illustrated as probability density functions. Here we classify pore-water as fresh for salinities below 1 psu, fresh to brackish for salinities ranging from 1 to 10 psu, and brackish for salinities ranging from 10 and 30 psu.

296 ### 3.4 Workflow calibration

297 We execute the above-outlined sequences to three key waypoints of the survey area. The
298 following steps are chronologically applied and presented:

299 1- Execute a Bayesian inversion at the waypoint located nearest to borehole U1353 (WP9 on
300 line 2) to verify, validate and calibrate our approach, where we have *in-situ* control.

301 We derive the PPD of resistivity at WP9, as illustrated in Figure 2b, and transform it to pore-
302 water salinity estimates (cf., Figure 4) using a) the porosity distribution over depth obtained from
303 the porosity-depth profile collected at the borehole and subsequently compare it to b) the
304 porosity estimates derived from the interpreted seismic facies (cf., Figure 3c).

305 2- Repeat the procedure at WP12 and WP60 along line 4, where the most prominent resistivity
306 anomaly is detected but no borehole data are available to constrain the pore-water salinity
307 conversion (cf., Figure 5 and Figure 6).

308 ## 4 Results

309 ### 4.1 CSEM-derived salinity conversion at borehole U1353

310 Figure 2a shows the 2-D inversion results of line 2 presented by Micallef et al. (2020).
311 The interface probability (left panel in Figure 2b) at WP9 (line 2) indicates that the CSEM data
312 can resolve two layers over a half-space with interfaces at approximately 14 and 80 mbsf. The
313 upper boundary of a subtle resistivity increase is well resolved, while the lower boundary is less
314 decisive, which is typical for CSEM resolution characteristics. The resistivity PPD (right panel in
315 Figure 2b) denotes that the resistivity of the upper two layers is well-constrained at 0.8 ± 0.5 and
316 2 ± 0.8 Ωm, respectively, down to approximately 80 mbsf. However, at greater depth, the
317 credibility intervals are wider, implying that the CSEM data do not constrain the model
318 resistivity beneath the second layer. The resistivity profile derived by the smoothed deterministic
319 2-D inversion at this location also shows changes in vertical resistivity-depth gradient. For the
320 second layer, the 2-D resistivities model coincides with the resistivity of the highest probability
321 in the Bayesian inversion. For the layer above and the region below the second layer, the 2-D
322 model predicts higher resistivities than the resistivities at the center of the probability
323 distribution, yet maintains the 95 percent credibility interval of the PPD.

The pore-water salinity probability density computed for porosity measurements taken in borehole U1353 (Figure 4a) shows a salinity-depth variation with decreased salinity values within the second layer. Above layer two, the predicted salinities approach normal seawater values. Below layer two, the range of possible salinities widens and ranges from brackish to hypersaline (> 30 psu) water. Yet, the highest probabilities are shown for seawater salinity of around 34 psu. The median pore-water salinity model follows the salinity trend over depth measured at the borehole (pink circular markers). The salinity profile converted from the 2-D inversion model fits well to the center of the salinity PPD for both borehole-based and seismically derived porosity estimates within the aquiferous layer. Salinity predictions based on porosity distribution extracted from interpreted seismic facies (Figure 4b) show almost identical results, validating that seismically derived porosities distributions are applicable to capture the *in-situ* porosity profile, particularly if we assume a Gaussian porosity distribution at each depth for seismic-derived porosities.

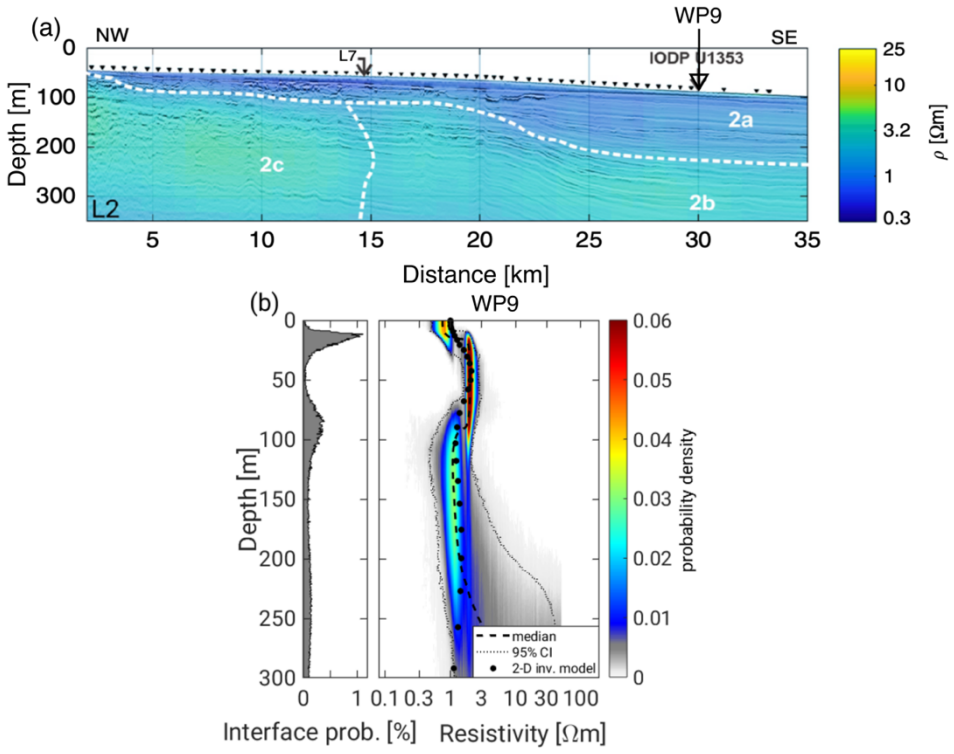

Figure 2. (a) 2-D resistivity model from the acquired CSEM data along line 2 as overlain on the corresponding seismic reflection profile (Micallef et al., 2020). Black triangles indicate stationary waypoints. The location of borehole U1353 and the closest waypoint (WP9) to that is marked by an arrow. (b) The result of 1-D Bayesian inversion at WP9. The left panel shows interface probability as a

function of depth. The right panel presents the resistivity marginal probability profile. The color indicates the probability. Credibility intervals contain 95 percent of the model samples evaluated at each depth interval. The 2-D resistivity model is shown by black circular markers.

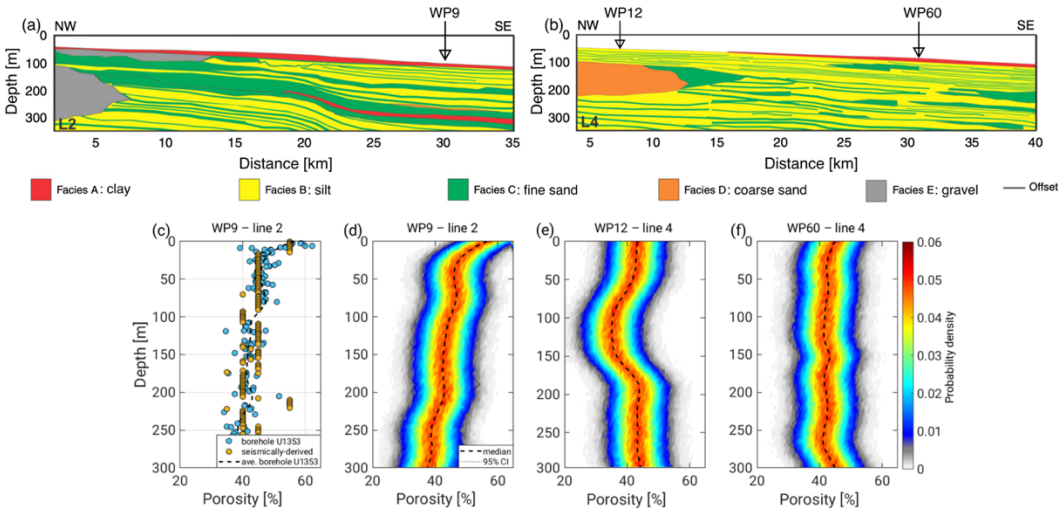

Figure 3. Seismically interpreted facies along (a) line 2 and (b) line 4 from Micallef et al. (2020). (c) Porosity profile measured at borehole U1353 (blue circular markers) and porosity profile extracted from interpreted facies (yellow circular markers) at the borehole location. The assumed probability distribution of porosities over depth at (d) WP9, (e) WP12, and (f) WP60.

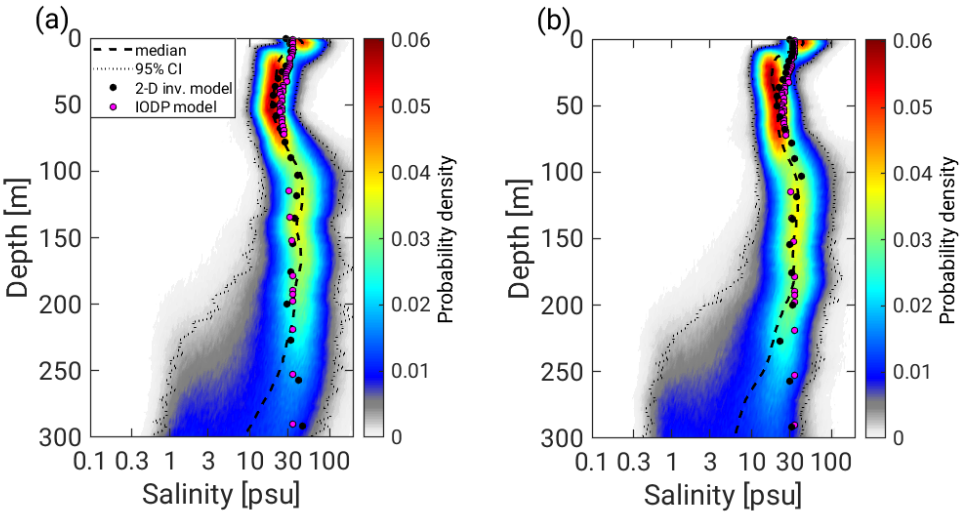

Figure 4. (a) Distribution of pore-water salinity as a function of depth at WP9 derived from Bayesian resistivity probability density (Figure 2b) by applying Archie's relationship using (a) porosities derived from *in-situ* measurements at U1353 and (b) porosities derived from interpreted seismic facies. Pore-

355 water salinity measurements at borehole U1353 and salinity estimates converted from 2-D inversion
356 resistivity models are shown in pink and black circular markers, respectively.

357 ### 4.2 Characteristics of salinity anomalies at the center of the survey area

358 The PPD of resistivity at WP12 in Figure 5b shows two well-identified interfaces at
359 depths of approximately 20 and 40 mbsf, each associated with a distinct increase in resistivity
360 reaching a maximum resistivity of around 200 Ωm in the third layer. The resistivity decreases
361 again at greater depths (with elevated interface probabilities between 110 and 200 mbsf). The
362 large range of resistivities at depths greater than 150 mbsf indicates a decrease in the sensitivity
363 of the data with the highest probabilities for resistivity values greater than 20 Ωm. In
364 comparison, the 2-D inversion model in Figure 5a shows only a continuous smooth increase in
365 resistivity with depth. While resistivities of the upper two layers and lower half-space coincide
366 with the median resistivity of the 1-D inversion results, the 2-D inversion model does not include
367 the highly resistive intermediate layer. We attribute the difference in resolution to the lower
368 minimum relative error of one percent assumed in the Bayesian inversion compared to the
369 minimum relative error of four percent applied in the deterministic 2-D inversion. This
370 hypothesis is corroborated by the fact that a rerun of the Bayesian inversion at WP12 with an
371 error level of four percent leads to a simple two-layer model consisting of a conductive layer
372 over a resistive half-space with no resistive anomaly (cf., Figure A 1a).

373 At WP60, the PPD of resistivity (Figure 5c) exhibits three layers over a half-space. The
374 Bayesian inversion places a resistive layer between 30 and 75 mbsf (with the highest probability
375 for a resistivity value of 15 Ωm) over a conductive layer (with resistivity values of less than 1
376 Ωm) between 75 and 100 mbsf. Note that the resistivity value within the underlying half-space is
377 poorly constrained, allowing for values greater than 3 Ωm. The 2-D inversion model at this
378 waypoint shows a smoothed version of the Bayesian-derived model, including the more
379 conductive layer at around 75 m depth.

380 Overall, we observe a decrease in resistivity values within our Bayesian resistivity
381 distributions from the near coastal site WP12 to the farther coastal site WP60.

382

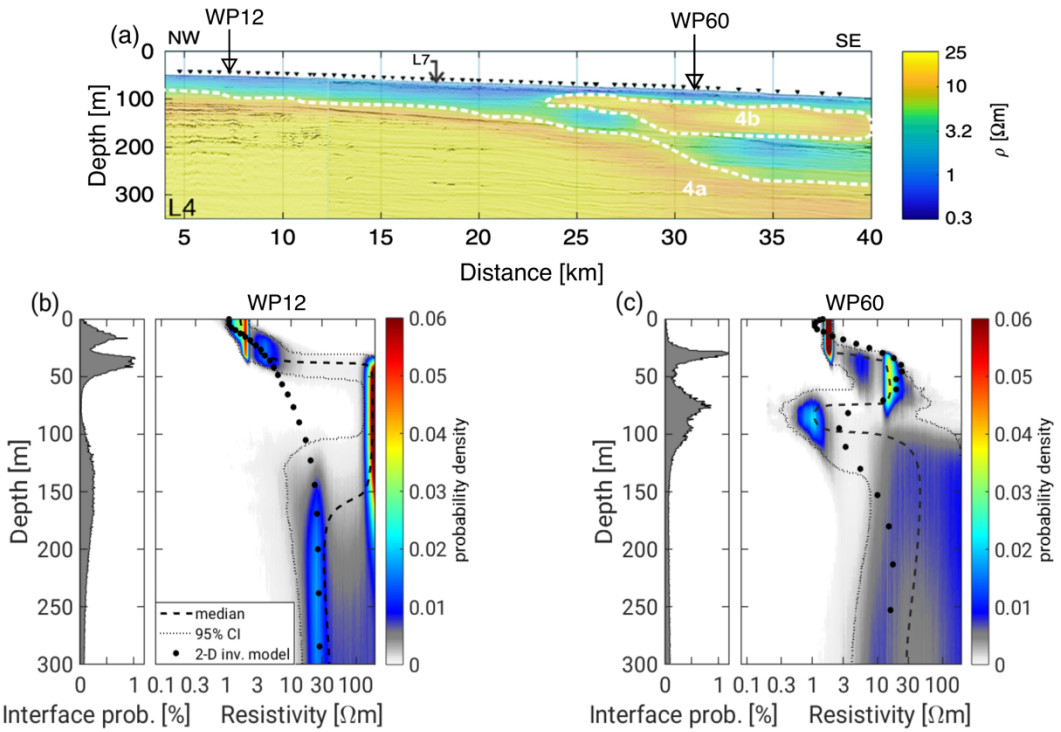

Figure 5. (a) 2-D inversion results along line 4 overlain on the seismic reflection profile (Micallef et al., 2020). Black triangles indicate the stationary waypoints. Left panels in (b) and (c) present interface probability at WP12 and WP60, respectively. The right panels in (b) and (c) illustrate probability density distributions of resistivity indicated by colors at WP12 and WP60, respectively.

The pore-water salinity distribution derived from the resistivity PPDs at WP12 (Figure 6a) indicates that the salinity values at the seafloor are around 34 psu, which is typical of the seawater salinity of the survey area. A layer of very low salinity appears between approximately 40 and 150 mbsf, with a thickness of 110 m and salinity variations between 0.1 and 0.5 psu indicating freshened pore-water. This layer of fresh pore-water roughly corresponds to the vertical extent of low-porosity (35 per cent) coarse-grained sand deposits in the interpreted seismic section (orange zone in Figure 3b). The correlation of the resistive anomaly with coarse sand structure further raises confidence in our results and that the CSEM data can resolve a layer with freshened pore-water when using an error level of one percent. At a depth between 110 and 200 mbsf, salinities increase (between 0.1 and 10 psu) indicating fresh to brackish pore-water, which extends to greater depths.

At WP60, there is a seawater-saturated shallow layer that is approximately 20 m thick, which is underlain by a low salinity layer extending down to about 75 mbsf. Pore-water salinity

in this layer is concentrated around 3 psu, suggesting the presence of a freshened zone between 25 and 75 mbsf (Figure 6b). Note that the depth interval of the freshwater zone occurs at a similar depth interval of the freshened groundwater body identified in the borehole on line 2. The freshened layer is followed by a highly saline layer between 75 m and 100 mbsf, with salinity values ranging between approximately 30 and 100 psu. Pore-water salinity decreases again at depths greater than 100 mbsf, showing a variation between 0.3 and 30 psu, suggesting a fresh to brackish groundwater body. These values are slightly higher than the predicted salinities within the lower freshwater body identified beneath WP12 at depths greater than 110 mbsf (Figure 6a).

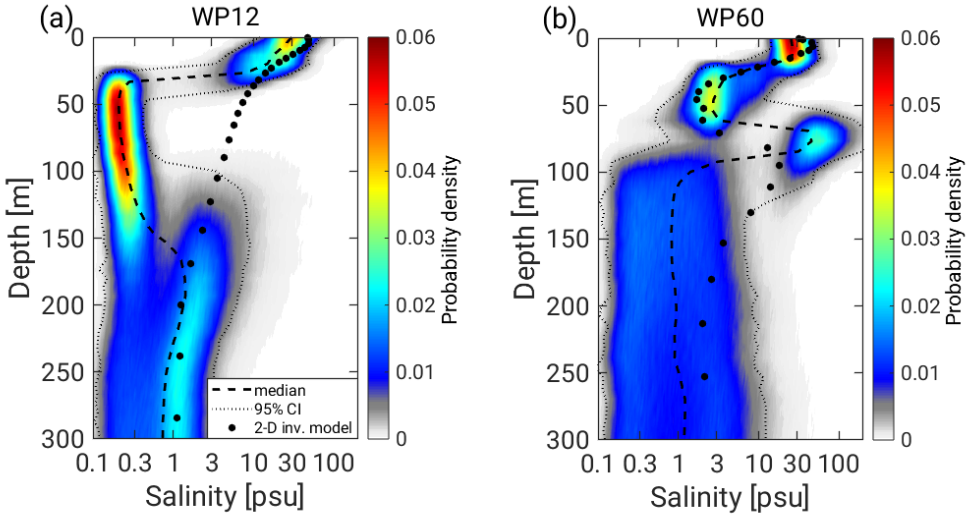

Figure 6. Probability distribution of pore-water salinity converted from posterior probability density at (a) WP12 and (b) WP60. The pore-water salinity distributions are derived based on the posterior probability density of resistivity (Figure 5b–c) and interpreted seismic facies derived porosity distributions at the respective waypoints (Figure 3e–f).

5 Discussion

Understanding salinity distributions of pore-fluid using CSEM data requires an understanding of electrical resistivity uncertainty, as well as a statistical analysis of the host-rock porosity and Archie's parameters. Deterministic inversion approaches fail to provide a quantitative uncertainty estimate of the resistivity. In contrast, Bayesian inversion algorithms result in PPD of resistivity, from which uncertainty in pore-water salinity estimates can be addressed. In this study, we present a workflow that converts sub-seafloor resistivity models to a

PPD of pore-water salinity by incorporating seismic attribute data and considering uncertainties in sediment porosity and Archie's parameters in equation (4).

5.1 Comparing 2-D deterministic and 1-D Bayesian inversion results

At the borehole location (WP9 of line 2), the probability distribution of resistivity and 2-D resistivity model coincide very well, which validates our 1-D Bayesian approach and enhances our confidence in the quality of the CSEM data. Similarly, at the eastern WP60 on line 4, where the resistivity cross-section along the profile exhibits 2-D resistivity variations, the PPD of resistivity shows good congruence with the 2-D inversion model indicating that the 1-D Bayesian approach can work in regions of temperate 2-D model variations. Surprisingly, at the western part of line 4 (WP12), where the sub-seafloor appears to be 1-D, there are clear disparities between the deterministic 2-D resistivity model and the probability distribution of resistivity between approximately 40 and 150 mbsf. The differences can be reconciled when applying a consistent minimum relative error of four percent in the Bayesian and 2-D inversion (cf., Figure A 1a). The resistivity model obtained from the 2-D inversion and the PPD of resistivity at WP12 in Figure A 1 show similar behavior, although the 2-D resistivity model indicates lower values as compared to resistivity estimates from Bayesian inversion. This shows that deterministic inversion approaches do not resolve sudden changes in resistivity due to the smoothing regularization of the method. The comparison between the probability distribution of resistivity depicted in Figure 5 with a minimum relative error of one percent and Figure A 1 with a minimum relative error of four percent reveals that the PPD of resistivity is highly dependent on the choice of error. Furthermore, increasing the data error leads to a decrease in model resolution. While we have verified the implementation of the one percent minimum relative error on data at the borehole location, it cannot be ascertained that we are not overfitting systematic errors in our data by choosing a small error of one percent compared to error estimates from stacking during CSEM data processing. The local error at one waypoint is usually smaller than the overall assumed error on the entire study area. Therefore, assuming a smaller minimum relative error and applying the Bayesian approach improves the model resolution. The difference between the probability distribution of resistivity and the 2-D model underlines the need for local, more stochastic inversion methods at points of interest identified by the 2-D inversion results. Nevertheless, a significant limitation of the Bayesian inversion approach is the high

computational time required to calculate the PPD. Consequently, this approach is currently only suitable for a few investigation points and is dependent on a multi-dimensional deterministic inversion to guide the choice of points for stochastic inversions.

5.2 Statistical derivation of pore-water salinity from PPD of resistivity

Estimating the pore-water salinity from the probability distribution of sub-seafloor resistivity is challenging due to uncertainties in Archie's coefficients. Borehole U1353 comprises lithological units that include interlayered clay, silt, and sand horizons, each characterized by different Archie's parameters (a and m in equation (4)). To address this issue, we adopt an approach in which we choose a uniform probability distribution for each of these parameters while converting the PPD of resistivity to the probability distribution of pore-water salinity. This approach results in broader salinity probability distributions (cf., Figure 4), allowing us to identify potential uncertainties due to our lack of detailed *in-situ* knowledge to calibrate Archie's parameters.

The salinity-depth measurements at borehole U1353 (indicated by pink circular markers in Figure 4) align with the high probability range of the predicted pore-water salinity distribution, although they do not coincide with the median salinity model. Specifically, salinities between 20 and 60 mbsf are higher compared to the salinity probability distribution's center, while salinities in the region below 120 mbsf are lower due to the presence of a different lithological unit (cf., Expedition 317 Scientists 2011). These results suggest that the uncertainty in Archie's parameters may impact the pore-water salinity estimation.

5.3 Correlation between pore-water salinity distribution and seismic facies

The agreement between the probability density distributions of pore-water salinity obtained from resistivity models employing seismically-derived porosity estimates and the *in-situ* porosity measurements at borehole U1353 (Figure 4a and Figure 4b) supports the suitability of using interpreted seismic facies for porosity estimation at distant locations from the borehole. It is important to note that the seismic facies classification needs to be extrapolated from a borehole and may lose accuracy at larger distances to the borehole.

The pore-water salinity PPD at the borehole location (WP9) overlaid on MCS line 2 demonstrates that the first and second interfaces at 14 and 80 mbsf correspond with two seismic

480 reflectors at the same depths (cf., Figure 7a). This alignment suggests that the salinity decrease
481 occurs within an onlap sedimentary package that comprises fine-grained sand, which is both
482 over- and underlain by fine silt and clay material. Towards the shore, the onlap sedimentary
483 package pinches out, making it unlikely that there is a connection or feeding mechanism from
484 current onshore groundwater bodies at U1353. In contrast, the sandy deposit extends horizontally
485 to the east. However, at borehole U1354, which is located approximately 8 km seaward of
486 U1353 along line 2, the subtle salinity variations are not detectable (cf., Figure 2c in Micallef et
487 al., 2020). Overall, the geometry of the sedimentary unit and estimated salinity variations suggest
488 that the freshened OFG body along line 2 is most likely a patchy remnant of a paleo groundwater
489 body that formed during previous glacial low stands (U1353 is located landward of the paleo-
490 shelf during the last glacial low stand). This remnant body may currently experience
491 salinification due to saltwater diffusion from the seaward side.

492 Line 4 presents salinity anomalies with greater variations and deeper depths compared to
493 line 2 (cf., Figure 2a and Figure 5a). Pore-water salinity PPD profile obtained from the eastern
494 part of line 4 (WP60) reveals the occurrence of a shallow freshwater zone between 15 to 70 mbsf
495 (cf., Figure 6b). This OFG body is located at a depth similar to the one observed at U1353, but
496 with significantly lower salinity values. The OFG body is situated within fine-grained sandy
497 sediments, which are underlain and overlain by clay and silty material. As with line 2, the
498 seismic reflector that corresponds to the upper limit of the sediment package pinches out
499 landwards. This observation is further supported by the 2-D resistivity section, which shows the
500 extension of the resistivity anomaly from approximately 24 km from the beginning of line 4 to
501 the end of the profile (Figure 5a). We interpret this feature as a remnant OFG body that likely
502 formed during the last (and possibly preceding) glacial seawater low-stand, similar to line 2. A
503 possible geological explanation for the zone of high conductivity is the presence of a clay-rich
504 sediment layer consisting of very fine-grained particles located directly beneath the shallow
505 OFG. However, we also acknowledge the possibility of inversion artifacts resulting from 2-D
506 effects, which could provide an alternative explanation.

507 At greater depths (> 100 mbsf) beneath WP60, a second low salinity layer has been
508 identified within silt/fine sand facies (Figure 6b). The upper limit of this OFG body coincides
509 with a seismic reflector located at approximately 100 mbsf, which is present throughout the
510 entire profile and rises landward (cf., Figure 7b). The Bayesian inversion results suggest that the

shallow and deep OFG bodies are not interconnected. This is further supported by both the 2-D inversion results and the seismic data, corroborating the absence of hydraulic continuity between these two distinct OFG bodies. The resolution of CSEM data decreases with depth and is limited below 100 mbsf, and as a result, we are unable to accurately constrain the depth of the base of the OFG body and variations in salinity at greater depths. Yet, our results indicate that pore-water salinities in this region are below 10 psu.

The deeper low-salinity body represents a somewhat different scenario from the shallower OFG bodies that are geometrically constrained and associated with onlap sediment packages. At the western part of line 4 (WP12), a freshwater OFG body with salinities below 0.5 psu is predicted between approximately 40 to 150 mbsf (cf., Figure 6a). This zone extends slightly above the top of a coarse sand sediment package (orange zone in Figure 3b), and is associated with a prominent seismic reflector that slopes eastwards along the profile, indicating the top of the deeper OFG body beneath WP60 (cf., Figure 7b). The base of the freshwater body is aligned with the base of the coarse-grained sand sediments at a depth of approximately 150 mbsf. Below the coarser sand zone, the pore-water salinity slightly increases while remaining in the freshwater range below 10 psu.

5.4 Interpreting an extensive OFG body

The correlation between the observed pore-water salinity variations at WP12 and WP60 ranging from 0.1 to 10 psu strongly suggests a hydraulic connection between the lower OFG body beneath WP60 and the freshwater OFG body to the west at WP12 (cf., Figure 7b). Our Bayesian inversion models, 2-D inversion results, and seismic data all support the possibility of a continuous freshwater body that may be hydrologically linked to a land-based aquifer. Although CSEM data is missing crossing the shallow water coastal transition zone, which would provide continuous coverage to confirm the land-sea groundwater connection, an EM/GPR study conducted along the Ashburton coast (north of line 4) by Weymer et al. (2020) that it is likely the onshore-offshore groundwater system is connected. The onshore aquifer is situated within gravel layers of sediment sequences (Dommisse, 2006) that were transported by high-energy braided rivers during the last glacial period (Rowan et al., 2012). Unconnected sand and silt/clay layers within these sequences serve as aquitards (Browne & Naish, 2003) Given that line 4 is located in an area with modern estuaries of various rivers (cf., Micallef et al., 2020), which are likely

remnants of the formerly high-energy braided rivers, and considering the seaward regional groundwater flow, it is plausible that the deep OFG body observed at line 4 is a continuation of the onshore aquifer extending seaward. Furthermore, onshore borehole information in the survey area (cf., Davey, 2004, 2006) provides approximate depths of the onshore multi-layer aquifers between 0 to 50 m, 50 to 90 m, and greater than 90 m. These depth ranges show a reasonable agreement with the depths of the OFG body along line 4 which strengthens the possibility of an onshore-offshore groundwater connection.

5.5 The impact of porosity variation on the pore-water salinity estimates

Porosity estimates for a sequence of silt and fine sand layers along line 4 based on interpreted seismic facies, are higher compared to those obtained from line 2 as there is a lack of borehole data for ground-truthing. To account for the uncertainty in porosity values, we integrate them into the pore-water salinity estimations by assuming normal distributions for seismically-driven porosity over depth. Yet, porosity estimates may vary beyond this range, especially at lithological transitions (e.g. between approximately 50 and 150 mbsf in Figure 3b and Figure 3e). A lower porosity associated with coarse sand units could result in higher salinities. To validate that the very low salinities observed are not due to high assumed porosity, we repeated the conversion of seafloor resistivity to pore-water salinity by reducing the porosity for the coarse sand facies by 15 percent (cf., Figure 8). The resulting PPD of pore-water salinity indicates slightly higher salinity values within the depth interval of the coarse sand layer (0.1 to 3 psu), yet still falls within the freshwater region. This is in agreement with Micallef et al. (2020), who concluded that the resistivity anomalies derived from 2-D inversion cannot be explained by porosity variations alone, but are indicative of freshened pore-water in the respective sediment sections.

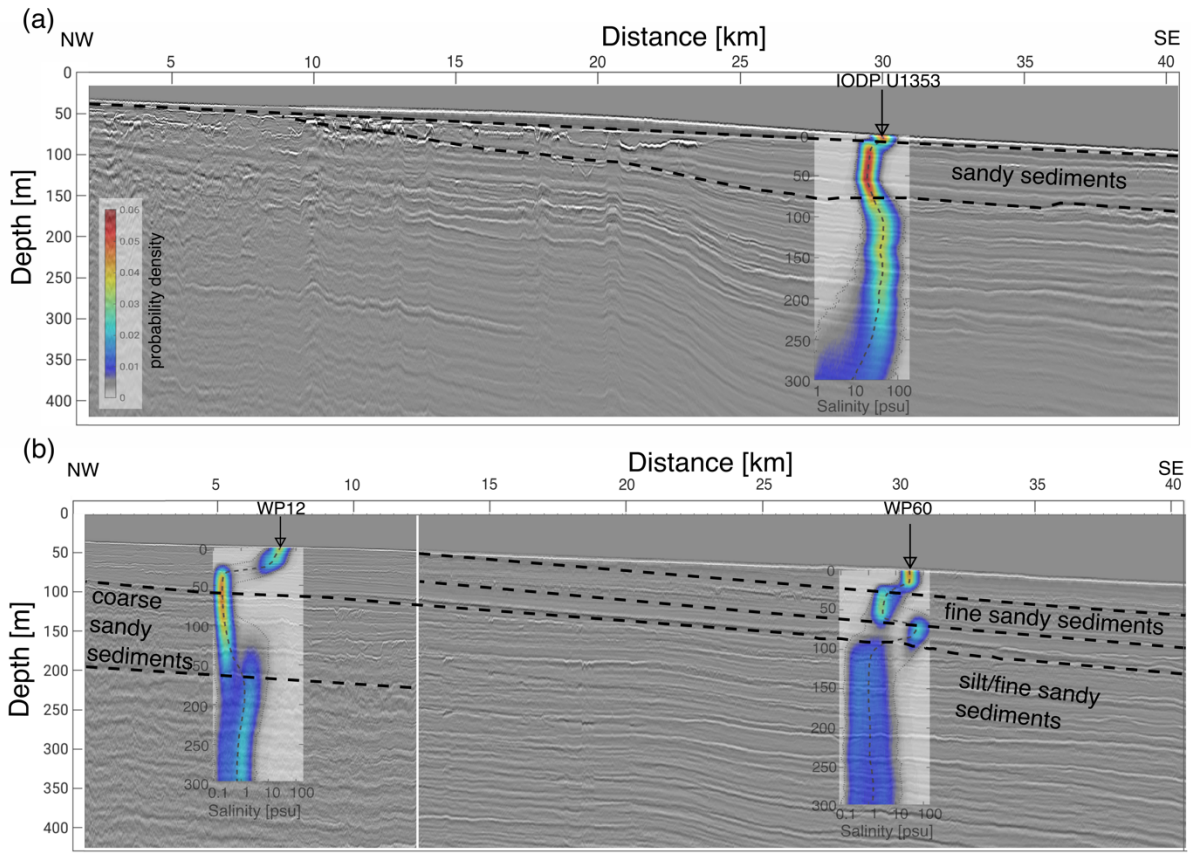

564

565 **Figure 7.** Seismic reflection data along (a) line 2 and (b) line 4 showing seismic reflectors. The white line
566 in (b) shows the boundary between two seismic profiles along line 4 acquired using different acquisition
567 equipment and geometry. Probability density distribution of pore-water salinity at (a) WP9 and (b) WP12
568 and WP60 overlain on the corresponding seismic lines.

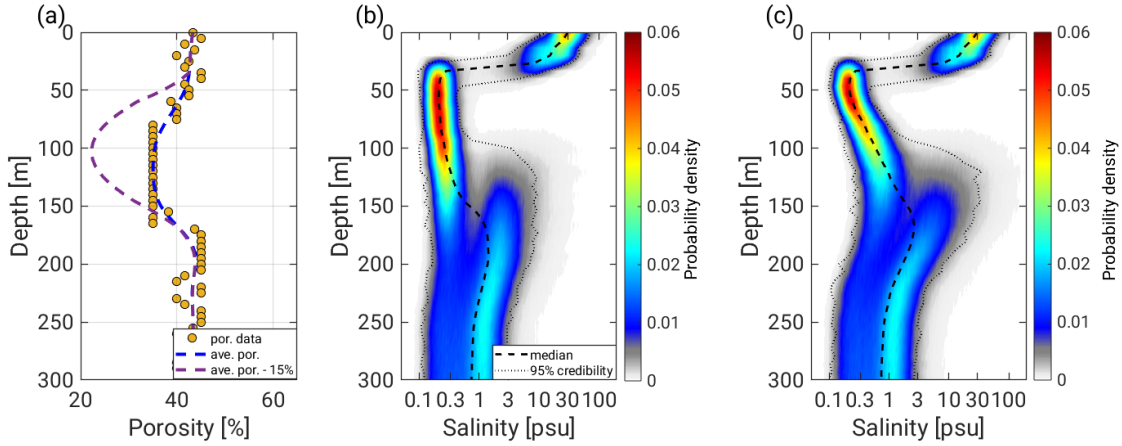

569

570 **Figure 8**. (a) An assumed 15 percent decrease in porosity within the depth range of coarse sand sediments
571 (indicated by the orange zone in Figure 3b) between approximately 50 and 150 mbsf. The corresponding

probability density distribution of pore-water salinity is calculated for a porosity value of (b) 35 percent and (c) 20 percent in the coarse-grained materials.

6 Conclusions

We present a methodology that employs a Bayesian workflow to evaluate uncertainty in pore-water salinity predictions within the Canterbury Bight. Our approach utilizes resistivity estimates obtained from CSEM data, in-situ porosity measurements, seismic-facies derived porosities, and Archie's rock physics relationship to characterize OFGs. We utilize a trans-dimensional MCMC algorithm to estimate a probability distribution of resistivity models and interface depth probabilities. By implementing Archie's relationship, we derive the pore-water salinity distribution and associated uncertainties from the resistivity models.

The efficacy of our workflow was successfully validated at the IODP borehole location, where it accurately captured a zone displaying a subtle drop in pore-water salinity values recorded in borehole U1353. Furthermore, our study reveals that interpreted seismic facies can serve as reliable proxies for classifying porosity estimates extrapolated from nearby boreholes.

In the center of the survey area, analysis of the correlation between the PPD of pore-water salinity and the seismic reflection profile along coast-perpendicular line 4 suggests the presence of an OFG body containing brackish to freshened pore-water stored within silty/fine-grained sediments at depths greater than 100 mbsf. Shoreward, the OFG body extends and transitions into facies comprising coarse sand sediments (west of line 4 at depths below 40 mbsf, Figure 7b). This freshened OFG likely represents an extension of the onshore aquifer and appears to be disconnected from a shallower local freshened zone identified in the eastern part of the profile.

To enhance our understanding of the extent of the salinity anomalies associated with freshened pore-water, we integrate them with stratigraphy derived from reflection seismic data. The trans-dimensional approach allows for the identification of abrupt resistivity changes related to freshened pore-water layers which helped to identify facies possibly connected to onshore groundwater that a 2-D deterministic approach overlooked. Therefore, we strongly recommend assessing uncertainties using Bayesian approaches for selected waypoints and estimating uncertainties for derived salinities to avoid both over and under-interpretation of the hydrogeological model such as the extent of groundwater within the seafloor.

Acknowledgments

This project has received funding from the European Research Council (ERC) under the European Union's Horizon 2020 research and innovation program (grant agreement No 677898; MARCAN). Ship-time aboard the R/V Tangaroa was partly funded by the New Zealand Ministry for Business Innovation and Employment through the Tangaroa Reference Group. Zahra Faghih and Amir Haroon received funding from the European Partnering Project SMART project (https://www.offshoregroundwater.com). The authors thank the captain, technicians, and scientific team members of the R/V Tangaroa for their support in data acquisition and processing during the TAN1703 cruise.

Open Research

The marine controlled source electromagnetic data and multi-channel seismic reflection data for this research are available at http://doi.org/10.5281/zenodo.8099305.

Access to the 1-D Bayesian inversion code is available upon request from Dr. Romina Gehrmann (RGehrmann@dal.ca).

References

Abubakar, A., Habashy, T., Druskin, V., Knizhnerman, L., & Alumbaugh, D. (2008). 2.5 D forward and inverse modeling for interpreting low-frequency electromagnetic measurements. *Geophysics*, *73*, F165–F177. https://doi.org/10.1190/1.2937466

Archie, G. E. (1942). The Electrical Resistivity Log as an Aid in Determining Some Reservoir Characteristics. *Transactions of the AIME*, *146*(01), 54–62. https://doi.org/10.2118/942054-G

Arévalo-Martínez, D. L., Haroon, A., Bange, H. W., Erkul, E., Jegen, M., Moosdorf, N., … Weymer, B. A. (2023). Ideas and perspectives: Land-ocean connectivity through groundwater. *Biogeosciences*, *20*(3), 647–662. https://doi.org/10.5194/bg-20-647-2023

Attias, E., Thomas, D., Sherman, D., Ismail, K., & Constable, S. (2020). Marine electrical imaging reveals novel freshwater transport mechanism in Hawai'i. *Science Advances*, *6*(48), eabd4866. https://doi.org/10.1126/sciadv.abd4866

Bakken, T. H., Ruden, F., & Mangset, L. E. (2012). Submarine Groundwater: A New Concept for the Supply of Drinking Water. *Water Resources Management*, *26*(4), 1015–1026. https://doi.org/10.1007/s11269-011-9806-1

Blatter, D., Key, K., Ray, A., Gustafson, C., & Evans, R. (2019). Bayesian joint inversion of controlled source electromagnetic and magnetotelluric data to image freshwater aquifer offshore New Jersey. *Geophysical Journal International*, *218*(3), 1822–1837. https://doi.org/10.1093/gji/ggz253

Bodin, T., & Sambridge, M. (2009). Seismic tomography with the reversible jump algorithm. *Geophysical Journal International*, *178*(3), 1411–1436. https://doi.org/10.1111/j.1365-246X.2009.04226.x

Browne, G. H., & Naish, T. R. (2003). Facies development and sequence architecture of a late Quaternary fluvial-marine transition, Canterbury Plains and shelf, New Zealand: implications for forced regressive deposits. *Sedimentary Geology*, *158*(1), 57–86. https://doi.org/https://doi.org/10.1016/S0037-0738(02)00258-0

Browne, G., & Naish, T. (2003). Facies development and sequence architecture of a late Quaternary fluvial-marine transition, Canterbury Plains and shelf, New Zealand: Implications for forced regressive deposits. *Sedimentary Geology*, *158*, 57–86. https://doi.org/10.1016/S0037-0738(02)00258-0

Cambareri, T. C., & Eichner, E. M. (1998). Watershed Delineation and Ground Water Discharge to a Coastal Embayment. *Groundwater*, *36*(4), 626–634. https://doi.org/https://doi.org/10.1111/j.1745-6584.1998.tb02837.x

Cohen, D., Person, M., Wang, P., Gable, C. W., Hutchinson, D., Marksamer, A., … Lane Jr., J. W. (2010). Origin and Extent of Fresh Paleowaters on the Atlantic Continental Shelf, USA. *Groundwater*, *48*(1), 143–158. https://doi.org/https://doi.org/10.1111/j.1745-6584.2009.00627.x

Constable, S. C., Parker, R. L., & Constable, C. G. (1987). Occam's inversion: A practical algorithm for generating smooth models from electromagnetic sounding data. *GEOPHYSICS*, *52*(3), 289–300. https://doi.org/10.1190/1.1442303

Davey, G. (2004). *Aquidef, a MS Access Programme to Define Canterbury Plains Aquifers and Aquitards. Environmental Canterbury Technical Report, No. U04/42.* Canterbury .

Davey, G. (2006). *Definition of the Canterbury Plains aquifers. Environmental Canterbury Technical Report, No. U06/10.*

Dettmer, J., & Dosso, S. E. (2012). Trans-dimensional matched-field geoacoustic inversion with hierarchical error models and interacting Markov chains. *The Journal of the Acoustical Society of America*, *132*(4), 2239–2250. https://doi.org/10.1121/1.4746016

Dettmer, J., Dosso, S. E., & Holland, C. W. (2011). Sequential trans-dimensional Monte Carlo for range-dependent geoacoustic inversion. *The Journal of the Acoustical Society of America*, *129*(4), 1794–1806. https://doi.org/10.1121/1.3557052

Dommisse, J. (2006). *Hydrogeology of the Hinds Rangitata Plain, and the Impacts of the Mayfield-Hinds Irrigation Scheme* (MSc thesis). University of Canterbury , Canterbury.

Dosso, S. E., Wilmut, M. J., & Lapinski, A. .-L. S. (2001). An adaptive-hybrid algorithm for geoacoustic inversion. *IEEE Journal of Oceanic Engineering*, *26*(3), 324–336. https://doi.org/10.1109/48.946507

Edwards, R. N. (1997). On the resource evaluation of marine gas hydrate deposits using sea-floor transient electric dipole-dipole methods. *GEOPHYSICS*, *62*(1), 63–74. https://doi.org/10.1190/1.1444146

Evans, R. (2007). Using CSEM techniques to map the shallow section of seafloor: From the coastline to the edges of the continental slope. *Geophysics*, *72*. https://doi.org/10.1190/1.2434798

Expedition 317 Scientists. (2011). In *Proceedings of the IODP, 317*. Integrated Ocean Drilling Program. https://doi.org/10.2204/iodp.proc.317.105.2011

Faghih, Z., Haroon, A., Jegen, M., Gehrmann, R., Schwalenberg, K., Micallef, A., Dettmer, J., Berndt, C., Mountjoy, J., & Weymer, B. A. (2023). Geophysical data - Canterbury Bight, New Zealand [Dataset]. Zenodo. https://doi.org/10.5281/zenodo.8099305

Fofonoff, N., & Millard, R. (1983). Algorithms for Computation of Fundamental Properties of Seawater. *UNESCO Tech. Pap. Mar. Sci.*, *44*.

Fulthorpe, C. S., Hoyanagi, K., Blum, P., Guèrin, G., & Scientists, E. 317. (2011). Expedition 317 Scientists, 2011. Site U1353. In *Proceedings of the IODP, 317*. Tokyo: Integrated Ocean Drilling Program. https://doi.org/10.2204/iodp.proc.317.105.2011

Gallagher, K. (2012). Transdimensional inverse thermal history modeling for quantitative thermochronology. *Journal of Geophysical Research: Solid Earth*, *117*(B2). https://doi.org/https://doi.org/10.1029/2011JB008825

Gehrmann, R., Dettmer, J., Schwalenberg, K., Engels, M., Dosso, S. E., & Özmaral, A. (2015). Trans-dimensional Bayesian inversion of controlled-source electromagnetic data in the German North Sea. *Geophysical Prospecting*, *63*(6), 1314–1333. https://doi.org/https://doi.org/10.1111/1365-2478.12308

Gehrmann, R., Schwalenberg, K., Riedel, M., Spence, G., Spiess, V., & Dosso, S. (2015). Bayesian inversion of marine controlled source electromagnetic data offshore Vancouver Island, Canada. *Geophysical Journal International*, *204*, 21–38. https://doi.org/https://doi.org/10.1093/gji/ggv437

Gelman, A., Carlin, J., Stern, H., Dunson, D., Vehtari, A., & Rubin, D. (2014). *Bayesian Data Analysis, 3rd Ed.*

Green, P. J. (1995). Reversible Jump Markov Chain Monte Carlo Computation and Bayesian Model Determination. *Biometrika*, *82*(4), 711–732. https://doi.org/10.2307/2337340

Gustafson, C., Key, K., & Evans, R. L. (2019). Aquifer systems extending far offshore on the U.S. Atlantic margin. *Scientific Reports*, *9*(1), 8709. https://doi.org/10.1038/s41598-019-44611-7

Haroon, A., Hölz, S., Weymer, B. A., Tezkan, B., & Jegen, M. (2018). *Calculating Time-Domain Controlled Source Electromagnetic Signals with MARE2DEM*. *2018*(1), 1–5. https://doi.org/https://doi.org/10.3997/2214-4609.201802663

Haroon, A., Lippert, K., Mogilatov, V., & Tezkan, B. (2018). First application of the marine differential electric dipole for groundwater investigations: A case study from Bat Yam, Israel. *GEOPHYSICS*, *83*(2), B59–B76. https://doi.org/10.1190/geo2017-0162.1

Haroon, A., Micallef, A., Jegen, M., Schwalenberg, K., Karstens, J., Berndt, C., … Chidichimo, F. (2021). Electrical Resistivity Anomalies Offshore a Carbonate Coastline: Evidence for Freshened Groundwater? *Geophysical Research Letters*, *48*(14), e2020GL091909. https://doi.org/https://doi.org/10.1029/2020GL091909

Hastings, W. K. (1970). Monte Carlo Sampling Methods Using Markov Chains and Their Applications. *Biometrika*, *57*(1), 97–109. https://doi.org/10.2307/2334940

Hathaway, J., Poag, C., Valentine, P., Manheim, F., Kohout, F., Bothner, M., … Sangrey, D. (1979). U.S. Geological Survey Core Drilling on the Atlantic Shelf. *Science (New York, N.Y.)*, *206*, 515–527. https://doi.org/10.1126/science.206.4418.515

Hoefel, F. G., & Evans, R. L. (2001). Impact of Low Salinity Porewater on Seafloor Electromagnetic Data: A Means of Detecting Submarine Groundwater Discharge? *Estuarine, Coastal and Shelf Science*, *52*(2), 179–189. https://doi.org/https://doi.org/10.1006/ecss.2000.0718

Hong, W.-L., Lepland, A., Himmler, T., Kim, J.-H., Chand, S., Sahy, D., … Knies, J. (2019). Discharge of Meteoric Water in the Eastern Norwegian Sea since the Last Glacial Period. *Geophysical Research Letters*, *46*(14), 8194–8204. https://doi.org/https://doi.org/10.1029/2019GL084237

Johnston, R. H. (1983). The saltwater-freshwater interface in the Tertiary limestone aquifer, southeast Atlantic outer-continental shelf of the U.S.A. *Journal of Hydrology*, *61*(1), 239–249. https://doi.org/https://doi.org/10.1016/0022-1694(83)90251-2

Key, K. (2016). MARE2DEM: a 2-D inversion code for controlled-source electromagnetic and magnetotelluric data. *Geophysical Journal International*, *207*(1), 571–588. https://doi.org/10.1093/gji/ggw290

King, R. B., Danskin, W. R., Constable, S., & Maloney, J. M. (2022). Identification of fresh submarine groundwater off the coast of San Diego, USA, using electromagnetic methods. *Hydrogeology Journal*, *30*(3), 965–973. https://doi.org/10.1007/s10040-022-02463-y

Levi, E., Goldman, M., Tibor, G., & Herut, B. (2018). Delineation of Subsea Freshwater Extension by Marine Geoelectromagnetic Soundings (SE Mediterranean Sea). *Water Resources Management*, *32*(11), 3765–3779. https://doi.org/10.1007/s11269-018-2018-1

Lippert, K., & Tezkan, B. (2020). On the exploration of a marine aquifer offshore Israel by long-offset transient electromagnetics. *Geophysical Prospecting*, *68*(3), 999–1015. https://doi.org/https://doi.org/10.1111/1365-2478.12875

Lu, H., & Fulthorpe, C. (2003). Three-dimensional architecture of shelf-building sediment drifts in the offshore Canterbury Basin, New Zealand. *Marine Geology*, *193*, 19–47. https://doi.org/10.1016/S0025-3227(02)00612-6

Malinverno, A. (2002). Parsimonious Bayesian Markov chain Monte Carlo inversion in a nonlinear geophysical problem. *Geophysical Journal International*, *151*(3), 675–688. https://doi.org/10.1046/j.1365-246X.2002.01847.x

Martin, J., Cable, J., Smith, C., Roy, M., & Cherrier, J. (2007). Magnitudes of submarine groundwater discharge from marine and terrestrial sources: Indian River Lagoon, Florida. *Water Resour. Res*, *43*. https://doi.org/10.1029/2006WR005266

Meisler, H., Leahy, P. P., & Knobel, L. L. (1984). The effect of eustatic sea-level changes on saltwater-freshwater relations in the northern Atlantic Coastal Plain. In *Water Supply Paper*. https://doi.org/10.3133/wsp2255

Metropolis, N., Rosenbluth, A. W., Rosenbluth, M. N., Teller, A. H., & Teller, E. (1953). Equation of State Calculations by Fast Computing Machines. *The Journal of Chemical Physics*, *21*(6), 1087–1092. https://doi.org/10.1063/1.1699114

Micallef, A., Person, M., Berndt, C., Bertoni, C., Cohen, D., Dugan, B., … Thomas, A. T. (2021). Offshore Freshened Groundwater in Continental Margins. *Reviews of Geophysics*, *59*(1). https://doi.org/10.1029/2020RG000706

Micallef, A., Person, M., Haroon, A., Weymer, B. A., Jegen, M., Schwalenberg, K., … Kumar Tiwari, A. (2020). 3D characterisation and quantification of an offshore freshened groundwater system in the Canterbury Bight. *Nature Communications*, *11*(1). https://doi.org/10.1038/s41467-020-14770-7

Mosegaard, K., & Tarantola, A. (1995). Monte Carlo sampling of solutions to inverse problems. *Journal of Geophysical Research: Solid Earth*, *100*(B7), 12431–12447. https://doi.org/https://doi.org/10.1029/94JB03097

Person, M., Dugan, B., Swenson, J. B., Urbano, L., Stott, C., Taylor, J., & Willett, M. (2003). Pleistocene hydrogeology of the Atlantic continental shelf, New England. *GSA Bulletin*, *115*(11), 1324–1343. https://doi.org/10.1130/B25285.1

Post, V., Groen, J., Kooi, H., Person, M., Ge, S., & Edmunds, W. (2013). Offshore fresh groundwater as a global phenomenon. *Nature*, *504*, 71–78. https://doi.org/10.1038/nature12858

753 Ray, A., Alumbaugh, D., Hoversten, G., & Key, K. (2013). Robust and accelerated Bayesian inversion of marine
754 controlled-source electromagnetic data using parallel tempering. *Geophysics*, *78*, 271-E280.
755 https://doi.org/10.1190/geo2013-0128.1
756 Ray, A., & Key, K. (2012). Bayesian inversion of marine CSEM data with a trans-dimensional self parametrizing
757 algorithm. *Geophysical Journal International*, *191*(3), 1135–1151. https://doi.org/10.1111/j.1365-
758 246X.2012.05677.x
759 Rowan, A. V, Roberts, H. M., Jones, M. A., Duller, G. A. T., Covey-Crump, S. J., & Brocklehurst, S. H. (2012).
760 Optically stimulated luminescence dating of glaciofluvial sediments on the Canterbury Plains, South Island,
761 New Zealand. *Quaternary Geochronology*, *8*, 10–22.
762 https://doi.org/https://doi.org/10.1016/j.quageo.2011.11.013
763 Sambridge, M, Gallagher, K., Jackson, A., & Rickwood, P. (2006). Trans-dimensional inverse problems, model
764 comparison and the evidence. *Geophysical Journal International*, *167*(2), 528–542.
765 https://doi.org/10.1111/j.1365-246X.2006.03155.x
766 Sambridge, Malcolm, & Mosegaard, K. (2002). MONTE CARLO METHODS IN GEOPHYSICAL INVERSE
767 PROBLEMS. *Reviews of Geophysics*, *40*(3), 3-1-3–29. https://doi.org/https://doi.org/10.1029/2000RG000089
768 Weymer, B. A., Everett, M. E., Haroon, A., Jegen-Kulcsar, M., Micallef, A., Berndt, C., … Post, V. (2022a). The
769 coastal transition zone is an underexplored frontier in hydrology and geoscience. *Communications Earth &*
770 *Environment*, *3*(1), 323. https://doi.org/10.1038/s43247-022-00655-8
771 Weymer, B. A., Wernette, P. A., Everett, M. E., Pondthai, P., Jegen, M., & Micallef, A. (2020). Multi-Layered High
772 Permeability Conduits Connecting Onshore and Offshore Coastal Aquifers. *Frontiers in Marine Science*, *7*.
773 https://doi.org/10.3389/fmars.2020.531293
774 Zamrsky, D., Essink, G. H. P. O., Sutanudjaja, E. H., van Beek, L. P. H. (Rens), & Bierkens, M. F. P. (2022).
775 Offshore fresh groundwater in coastal unconsolidated sediment systems as a potential fresh water source in the
776 21st century. *Environmental Research Letters*, *17*(1), 014021. https://doi.org/10.1088/1748-9326/ac4073
777 Zamrsky, D., Karssenberg, M. E., Cohen, K. M., Bierkens, M. F. P., & Oude Essink, G. H. P. (2020). Geological
778 Heterogeneity of Coastal Unconsolidated Groundwater Systems Worldwide and Its Influence on Offshore
779 Fresh Groundwater Occurrence. *Frontiers in Earth Science*, *7*. Retrieved from
780 https://www.frontiersin.org/articles/10.3389/feart.2019.00339

781

782 Appendix A: PPD of Resistivity for a Minimum Relative Error of Four Percent

783 To assess the impact of error models on the PPD of resistivity obtained through Bayesian
784 inversion, we perform additional Bayesian inversions at WP12 and WP60 using a minimum
785 relative error of four percent, as applied by Micallef et al. (2020). Figure A 1 illustrates the
786 Bayesian inversion results at WP12 and WP60 in terms of interface-depth probabilities and the
787 marginal probability density profile of the resistivity. The probability distribution of resistivity at
788 WP12 only resolves the first interface at 25 mbsf, indicating a significant increase in resistivity
789 to values greater than 100 Ωm. Overall, the data lose resolution at greater depths. At WP60, the
790 PPD of resistivity shows three distinct layers above the basement, which agrees well with the 2-
791 D inversion model. Nevertheless, interface probabilities as a function of depth suggest only one
792 distinct interface at 50 mbsf with high uncertainty.

793

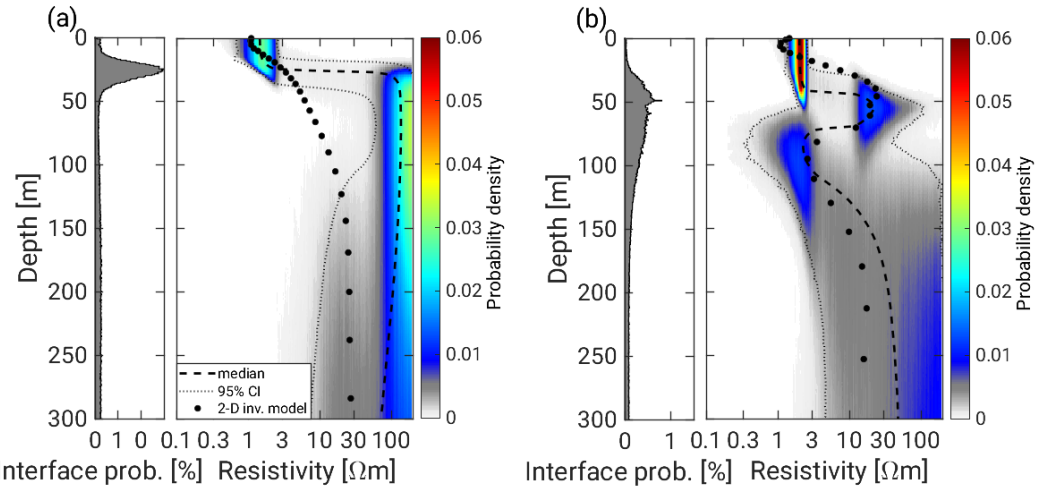

794

795 **Figure A 1.** Probability density distributions of sub-seafloor resistivity at (a) WP12 and (b) WP60
796 assuming a minimum relative error of four percent, as it was assumed for 2-D deterministic inversion of
797 CSEM data at the same waypoints.

798